

Sustainable Energy & Fuels

Interdisciplinary research for the development of sustainable energy technologies

rsc.li/sustainable-energy



ISSN 2398-4902

Product analysis

The reaction samples were centrifuged first to separate any residual catalyst particles and the liquid phases obtained were analyzed by GC-MS (Agilent 7890-5977A, Agilent). The GC was equipped with an HP-5 column (30 m × 250 μm × 0.25 μm), and a Flame Ionization Detector (set point was 608 K). The injector temperature was kept at 608 K. The initial oven temperature was 373 K for 1 min which was heated at 10 K min⁻¹ to 463 K where ramping continued at 30 K min⁻¹ to 673 K where it was held constant for 1.3 min. External calibrations were used for the quantification of the intermediates and products. Since 2,2'-biphenol is insoluble in dodecane at room temperature ethanol was added to the calibration and reaction samples prior to analysis to solubilize 2,2'-biphenol. The conversion of the reactant and selectivity for the products were calculated for each experiment using the following equations:

$$\text{Conversion, } X \text{ (\%)} = \left(1 - \frac{\text{moles of reactant left}}{\text{initial moles of reactant}}\right) \times 100$$

$$\text{Yield (\%)} = \frac{\text{moles of product}}{\text{moles of reactant charged}} \times 100$$

$$\text{Selectivity (\%)} = \frac{(\text{moles of product})_i}{\sum_i (\text{moles of product})_i} \times 100$$

Catalyst characterization

The textural properties of the synthesized and spent catalysts were determined by using nitrogen physisorption isotherms using a TriStar 3000 gas adsorption analyzer. The NiMoA samples were dried at 250 °C for 2 h in a flow of dry N₂, Zeolite containing samples were dried for 6 h. The specific surface area was calculated based on the Brunauer–Emmett–Teller equation (BET). The pore size was estimated based on the desorption isotherm using the Barrett–Joyner–Halenda equation (BJH). To verify the metal contents, the fresh and recovered catalysts after the reaction were analyzed by Inductively Coupled Plasma (ICP)-Sector Field Mass Spectroscopy (ICP-SFMS) by ALS Scandinavia AB, Luleå, Sweden. C, H, N and S elemental analysis on the recovered catalysts was carried out by Elemental Microanalysis Ltd. (UK) using EA-1110 (CE Instruments) and NA2000 (Fisons Instruments) elemental analyzers.

Ethylamine temperature programmed desorption (TPD) experiments were performed in an arrangement consisting of a manifold of mass flow controllers (MFCs) for feed gas mixing, a quartz tube containing the catalyst sample (approximately 25 mg) in a temperature-controlled oven and a mass spectrometer (Hiden HPR-20 QUI) for measuring the quantities of desorbed products in the outlet carrier gas. The samples were initially pretreated in Ar (110 °C for 1 h and 250 °C for 3 h) followed by reduction in a flow of 13% H₂ at 600 °C for 2 h and thereafter cooling to 100 °C in Ar. After flow stabilization in Ar, the sample was exposed to 543 ppm of

ethylamine at 100 °C for 3 h. Then, the sample was flushed with Ar for 2 h followed by desorption with a ramp rate of 5 °C min⁻¹ to 600 °C. The total gas flow rate was maintained at 20 NmL min⁻¹ through the quartz tube containing the sample.

The X-ray diffraction (XRD) pattern of the synthesized catalysts was obtained using a Bruker AXSD8 Advance X-ray powder diffractometer with CuKα radiation (λ = 1.542 Å). Scanning parameters of 2θ were from 5 to 80° in the scan mode (0.03° and 1 s). Raman scattering spectroscopy (WITec alpha300 R, 532 nm laser, 75 mW) was used to characterize the Mo–O bond in the supported catalysts. X-ray Photoelectron Spectroscopy (XPS) studies on sulfided catalysts were performed using a PerkinElmer PHI 5000 VersaProbe III Scanning XPS Microprobe. The sample was irradiated with a monochromatic Al-Kα source with a binding energy of 1486.6 eV in a vacuum chamber (less than 2 × 10⁻⁸ torr). The emitted photoelectrons were detected by using a spherical energy analyzer. The angle between the source and detector was 90°. High resolution spectra with a step of 0.10 eV were recorded for Ni, Mo, O, S and C core levels. Data obtained were analyzed by using Multipack software and with CasaXPS. For all spectra the C 1s binding energy of 284.6 eV was taken as the reference.

Transmission electron microscopy (TEM) analysis was performed using a FEI Titan 80-300 TEM operating at an accelerating voltage of 300 kV. Scanning TEM (STEM) images were acquired using a high angle annular dark field (HAADF) detector. In the STEM mode, energy dispersive X-ray (EDX) analysis was also performed for chemical identification using an Oxford X-sight detector. Spectrum acquisition and data analysis were performed using TEM Imaging & Analysis (TIA) software. Ni promoted MoS₂ crystallites were measured by using ImageJ software and at least 300 slabs were taken to calculate the surface average length and stacking using the first moments of the distribution:⁵⁶

$$\text{Average slab length} = \frac{\sum_i^n n_i l_i}{\sum_i^n n_i}$$

$$\text{Average stack number} = \frac{\sum_i^n n_i N_i}{\sum_i^n n_i}$$

where n_i is the number of slabs having length l_i and N_i is the number of layers in slab i .

Furthermore, the MoS₂ dispersion denoted as f_{Mo} , was measured based on the average fraction of Mo atoms at the MoS₂ edge surface assuming that MoS₂ slabs have a perfect hexagonal shape.

$$f_{\text{Mo}} = \frac{\text{Mo}_{\text{edge}}}{\text{Mo}_{\text{total}}} = \frac{\sum_i^m 6(n_i - 1)}{\sum_i^m (3n_i^2 - 3n_i + 1)}$$

where Mo_{edge} is the number of Mo atoms at the edges of MoS₂ slabs, Mo_{total} denotes the total number of Mo atoms and n_i the



number of Mo atoms at the edge of one MoS₂ slab which can be determined from its length, $L = 3.2(2n_i - 1) \text{ \AA}$, and m is the total number of slabs.

Results and discussion

HDO of BPE

Fig. 2 presents the products and intermediates formed during the HDO of BPE. Selective hydrogenolysis of the C_{aliphatic}-O bond (α -O-4) in BPE primarily yields toluene and phenol.⁵⁷ On the other hand, the acid catalyzed transalkylation reaction *via* the transfer of the benzyl group in BPE leads to the formation of benzyl phenols.¹³ As reported in the literature, recombination of hydrogenolysis and hydrolysis intermediates may also form benzyl phenols and other dimers linked *via* C-C bonds as

presented in Fig. 2(c).³⁴ However, transalkylation seems to be the dominant path to form benzyl phenols as the peak in their formation coincides with when full conversion of BPE occurs. Fig. 2(c) illustrates all the components identified by GC-MS analysis of the samples in a proposed reaction scheme. It is important however to note that benzyl alcohol (faint print in Fig. 2(c)) was not detected. This suggests that the recombination pathway is of lesser importance or that benzyl alcohol is rapidly consumed when formed. The catalysts containing Y-zeolite have enhanced rates of hydrogenolysis as shown in Fig. 2(a). Approximately, 80–90% conversion of BPE occurs in 0.5 h for catalysts with Y-zeolite. This is likely due to increased rates of the transalkylation and hydrolysis reactions of BPE with the more acidic catalysts. The phenolics thus formed undergo HDO, HYD, isomerization and hydrocracking to yield a mixture

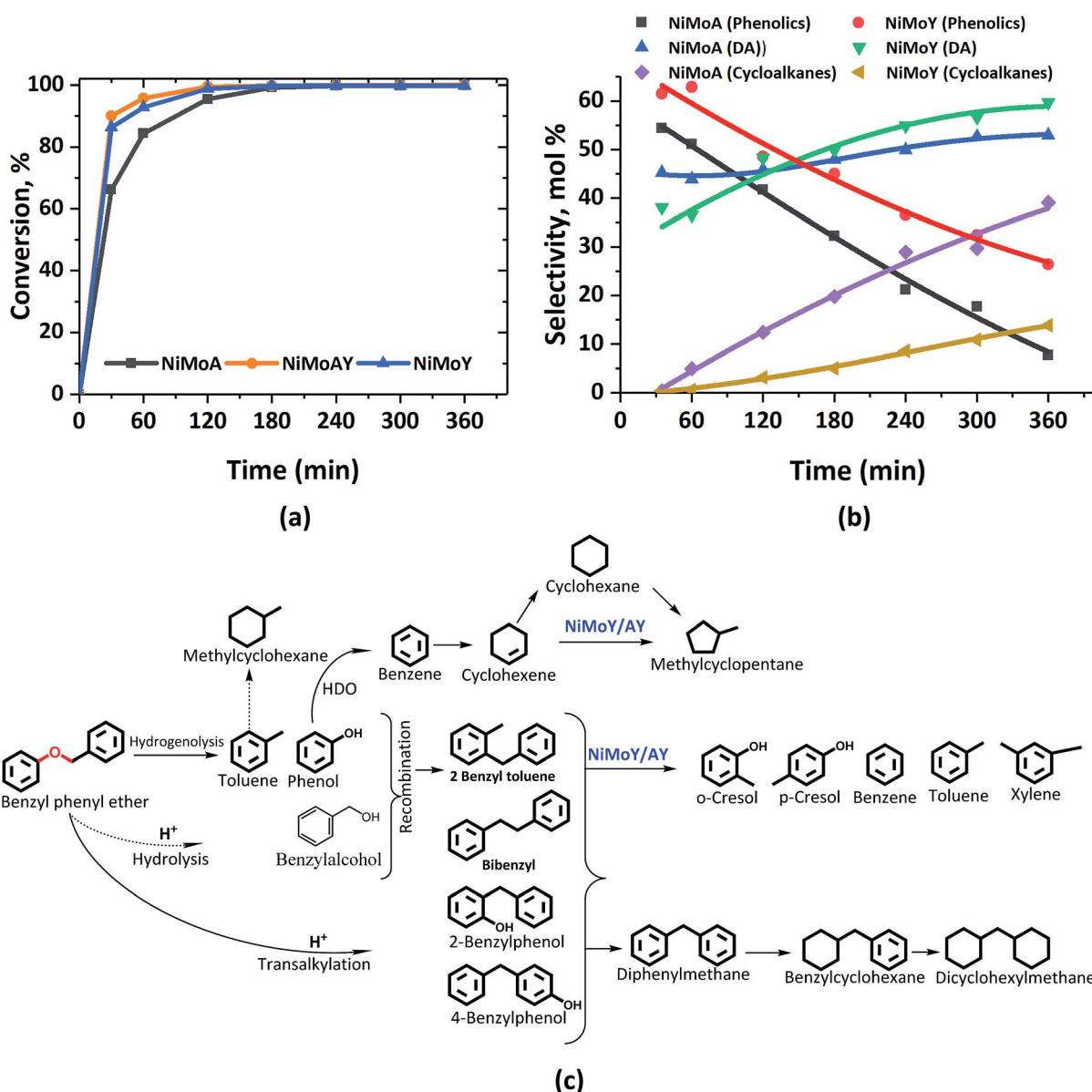


Fig. 2 (a) BPE conversion and (b) product selectivity during HDO of BPE in an autoclave at 593 K, 5 MPa and 1000 rpm. (c) Proposed reaction scheme. DA = deoxygenated aromatics.



of deoxygenated aromatics and alicyclics. For simplicity products are grouped into phenolics, deoxygenated aromatics (DA) and cycloalkanes to show their reaction time profiles in Fig. 2(b). Based on the time evolution of these products and intermediates, the reaction scheme in Fig. 2(c) is proposed. The selectivity for phenol and benzyl phenol intermediates was observed to increase first and later decrease, whereas the selectivity for the final products increased with time (Fig. S1†). Table 1 shows the major compounds included in each of these groups and details of the final product selectivity.

As can be seen from Fig. 2(b), phenolics deoxygenation is faster without Y-zeolite but with greater formation of methylene/ethylene linked C–C dimers with partial or full hydrogenation of the benzene rings (Fig. 2(c)). The formation of such C–C dimers will be illustrated and discussed further. Interestingly, sulfided NiMoY yields higher DA due primarily to high benzene formation as shown in Table 1 for the final products. Also, even at the same selectivity for phenolics, *e.g. ca.* 40%, it can be seen in Fig. 2(b) that the selectivity for DA products was higher at 50% for NiMoY, compared to 45% for NiMoA. The results in Table 1 indicate that dimer (phenolics or DA) formation after full reaction time is significantly lower on NiMoY owing to promoted C_{aryl}–C_{aliphatic} bond cleavage of the benzyl phenols, diphenylmethane (DPM), bibenzyl (BB) and others. This facilitates the formation of monoaromatics comprising cresols, benzene, toluene and xylene (BTX). Güvenatam *et al.*³⁴ reported that acidic conditions lower the side reactions to dimers/trimers in the presence of H₂ during HDO of BPE on Pt/C. H₂-driven cracking of benzyl phenols, DPM and BB was previously reported for Fe, Ni and Mo-based catalysts at elevated temperatures and pressures.^{32,58} Koyama *et al.*³² reported considerable dimer formation while hydrocracking lignin dimers (BPE, diphenyl ether, benzyl phenols, diphenylmethane and dibenzyl) without solvent in a temperature range of 340–450 °C. The extent of C–C cleavage reported for DPM and BB was low at 420 °C but significant for BB at 450 °C. In this study no C–C cleavage of the yielded dimers was observed for NiMoA; however it was observed to a small extent on NiMoAY. Indeed, an increased selectivity for dimer products was observed for NiMoA (*discussed in the section 'Catalytic properties related to the activity'*), whereas for NiMoY the selectivity for these products peaked at 1 h and then declined. Improved C–C bond cleavage with NiMoY

opens up the possibility to valorize technical lignin in biorefinery processes.⁴⁰

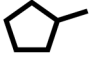



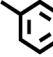

Interestingly, a high hydrogenation activity yields more cycloalkanes over sulfided NiMoA than NiMoY (Fig. 2(b)). For example, 38% cyclohexane is found for NiMoA, while it is <1% for NiMoY, which instead produced 35% benzene. Methyl-cyclopentane observed primarily with NiMoAY and NiMoY (Table 1) indicates the greater isomerization activity of these catalysts due to the higher concentration of Brønsted acidic sites in the zeolite pores promoting greater isomerization activity.⁵⁹

HDO of PPE

Fig. 3 shows the formation of phenolics, DA and alicyclics during the HDO of PPE. H₂-driven hydrogenolysis of the sp³ C–O bond (β-O-4) to ethylbenzene and phenol is fastest in this case over NiMoAY, whereas the rate of conversion of PPE is slowest for NiMoY as shown in Fig. 3(a). The details of the final product selectivity are shown in Table 2. Fig. 3(c) illustrates all of the observed components in a proposed reaction scheme. Similar to the case of BPE, note however that the phenethyl alcohol (faint print in Fig. 3(c)) intermediate that would be consumed by the recombination reactions was not detected. Transalkylation of the phenethyl group of PPE and recombination reactions are favored in the order of NiMoY > NiMoAY > NiMoA, leading to the formation of high quantities of phenolic dimers as mainly phenylethyl phenols having ethylene linked C–C bonds (Fig. 3(c)). Like with BPE, such dimers undergo C–C cleavage over NiMoY to yield ethyl phenols. The formation and cleavage of such C–C dimers will be further compared in the section '*Catalytic properties related to the activity*'. However, deoxygenated aromatics including benzene, toluene, ethylbenzene and a small number of dimers (Fig. 3(b) and Table 2) increase as the reaction progresses. Based on the evolution of these products and intermediates (Fig. S2†), a reaction scheme shown in Fig. 3(c) is proposed.

Clearly, the degree of HDO selectivity is very high with NiMoA, whereas isomerization and hydrocracking increase with NiMoY/AY. Hydrogenation activity seems lower for NiMoY leading to high monoaromatics selectivity (>80%) as with BPE, however at the expense of an even lower rate of conversion of phenolics compared to BPE (Fig. 3(b)). Noticeably, as shown in Table 2, selectivity for cycloalkane products is almost four times

Table 1 Product selectivity's from HDO of BPE after a 6 h reaction at 5 MPa and 593 K^a

Catalyst	X _{BPE} (%)	Carbon balance (%)	Selectivity (%)									
			Cycloalkanes			Deoxygenated aromatics (DA)			Phenolics			
					Others				Dimers		Cresols	Dimers
NiMoA	>99	94	<1	38	1	—	43	—	9	7	—	2
NiMoAY	>99	92	2.7	28	3.5	—	44	0.5	5	13	2	0.7
NiMoY	>99	87	9.3	<1	4.5	35	22	2	—	18	8	0.4

^a X_{BPE} refers to BPE conversion.





Fig. 3 (a) PPE conversion and (b) product selectivity during HDO of PPE in an autoclave at 593 K, 5 MPa and 1000 rpm. (c) Proposed reaction scheme. DA = deoxygenated aromatics.

lower with NiMoY due to a noteworthy drop in hydrogenation activity compared to NiMoA.

Compared to BPE, the cleavage of PPE and PPE derived-dimers seems hindered by the USY pore sizes, particularly its micropores. The presence of such bulkier molecules may hinder

the monophenol HDO due to preferential adsorption of the reactant/intermediates which may aid undesirable secondary reactions to build carbonaceous deposits that can deactivate the catalyst with increasing reaction time.

Table 2 Product selectivity's from HDO of PPE after a 6 h reaction at 5 MPa and 593 K^a

Catalyst	X_{PPE} (%)	Carbon balance (%)	Selectivity (%)									
			Cycloalkanes			Deoxygenated aromatics (DA)			Phenolics			
					Others				Dimers	Ethyl-phenols	Dimers	
NiMoA	>99	95	—	45	3	—	—	48	3	1	—	1
NiMoAY	>99	93	17	16	3	—	—	48	3	12.5	—	3
NiMoY	>99	84	10	—	1.5	14	1	32.5	2	31	4	4

^a X_{PPE} refers to PPE conversion.



HDO of 2,2'-biphenol

Table 3 shows the final product selectivities for 2,2'-biphenol HDO. After 6 h of reaction at 5 MPa and 593 K, 91% conversion of 2,2'-biphenol was observed over NiMoA while for Y-zeolite containing catalysts it was above 99% (Table 3). Fig. 4(b) shows the complete range of products observed and illustrated in a proposed reaction scheme. The mass balance was poor for the early samples (before 180 min) for NiMoA probably due to the low solubility of the reactant in dodecane at room temperature or residual reactant remaining in the sampling line. However, it became >90% for the latter samples. Fig. 4(a) compares the selectivity for the major products for NiMoA and the zeolite containing catalysts. As can be seen in Fig. 4(a), for all catalysts, the acid catalyzed dehydration reaction leads to the formation of dibenzofuran (DBF) *via* intramolecular nucleophilic attack of the hydroxyl group.³³ DBF formation competes with HDO over NiMoA to form *o*-phenylphenol (OPP). Over sulfided NiMoA hydrogenation of DBF produces tetrahydro-dibenzofuran (THDBF) which followed by C–O cleavage gives 2-cyclohexylphenol (CHPOH). *Para* and *meta* substituted cyclohexylphenol were also observed to a small degree. Further HDO and HYD of CHPOH lead to the formation of several components shown in Fig. 4(b). Biphenyl (BP) formation was quite low indicating the C–O cleavage of CHPOH leading to the formation of cyclohexylbenzene (CHB). Sulfided NiMoA eventually breaks the C–C linkage of CHPOH/CHB to phenol and cyclohexane with substantial cyclic dimers including bicyclohexane (BCH) and cyclopentyl-cyclohexylmethane (CPMCH). From Table 3, it is clear that 36% dimers have been formed with NiMoA. These observations are in line with the previous studies of DBF hydrotreatment over sulfided NiMoA.⁶⁰ Also, similar product formation was reported for HDO of DBF using a Pt based catalyst over various acid–base supports.^{61–64}

For the Y-based catalysts, the dehydration reaction is strongly favoured over DDO resulting in a high yield of DBF which is over 44%, compared to 23% with NiMoA (Table 3). As Fig. 4(a) shows that the conversion of 2,2'-biphenol to DBF occurs quickly and was complete already during the process of heating the reactor to 593 K. Also, for the Y-based catalysts, no OPP was identified in the early samples taken during the experiments. However, the cleavage of the C–O bond in the recalcitrant DBF seems to become the rate determining step, particularly for the Y-zeolite containing catalysts. Once the C–O

bond is cleaved, traces of intermediates (*e.g.* biphenyl, 1-phenyl cyclohexene, *etc.*) in the reaction mixture appear, which undergo rapid acid induced cracking inside the zeolite pores. This leads to the formation of phenol and cyclohexane as the cracking products. Further isomerization of cyclohexane yielded methyl-cyclopentane at over 39% with the zeolite catalysts compared to only residual quantities with NiMoA (Table 3). Also, with the zeolite catalyst no formation of other C–C dimers was detected (Table 3). Moreover, the reaction with the support USY only primarily yields DBF and its derivatives (*e.g.* 9-hydroxyfluorene, 9,9 dimethylxanthene, *etc.*) and a small amount of methylcyclopentane (~8%) and phenol (~6%) (Fig. S3†). This indicates a strong synergy between the active NiMoS phase and the acidity of the support which cleaves C–O and C–C faster. And for the reaction with γ -Al₂O₃, approximately 40% of feed was converted exclusively to DBF. Since NiMoY yielded more coke in the first run (Table 7) we repeated the experiments with the recovered catalysts from the first run in the same fashion. The results (Fig. S4†) indicate a small drop in the catalytic activity of the catalyst.

In summary, with the zeolite-based catalysts the initial formation of DBF was almost exclusively favoured, due to the stronger acidity of these catalysts promoting dehydration reactions, whereas with NiMoA formation of THDBF, OPP and various other products from it was also important. All catalysts had difficulty to further convert the recalcitrant DBF. As a result, for the zeolite-based catalysts the products after complete reaction time contained higher quantities of DBF; however their better activity for C–C cleavage reactions caused their products to be free of detectable amounts of dimers (Table 3).

Catalyst characterization

ICP-SFMS data in Table 4 show the metal contents and Si/Al ratios (SARs) of the zeolite framework. A slight variation in the SAR has been noticed after Ni and Mo impregnation into the Y zeolite and for the recovered catalyst after the activity test; however this is within the expected measurement variation. The Ni/(Ni + Mo) content seems consistent for the synthesized and spent catalysts. Hence, leaching of Ni and Mo can be ruled out.

The acidity of the catalysts was measured by ethylamine (C₂H₅NH₂) TPD and is presented in Fig. 5 and Table 5. An advantage of using ethylamine is that it measures the Brønsted acidity directly whereas the more common NH₃-TPD requires

Table 3 Product selectivity's from HDO of 2,2'-biphenol after 6 h of reaction at 593 K, 5 MPa and 1000 rpm^a

Catalyst	X _{5-5'} (%)	C-balance (%)	Selectivity (%)				Dimers
							
NiMoA	91	95	23	4	36	<1	36
NiMoAY	>99	94	59	2	—	39	—
NiMoY	>99	96	44	13	—	43	—

^a X_{5-5'} refers to 2,2'-biphenol conversion.



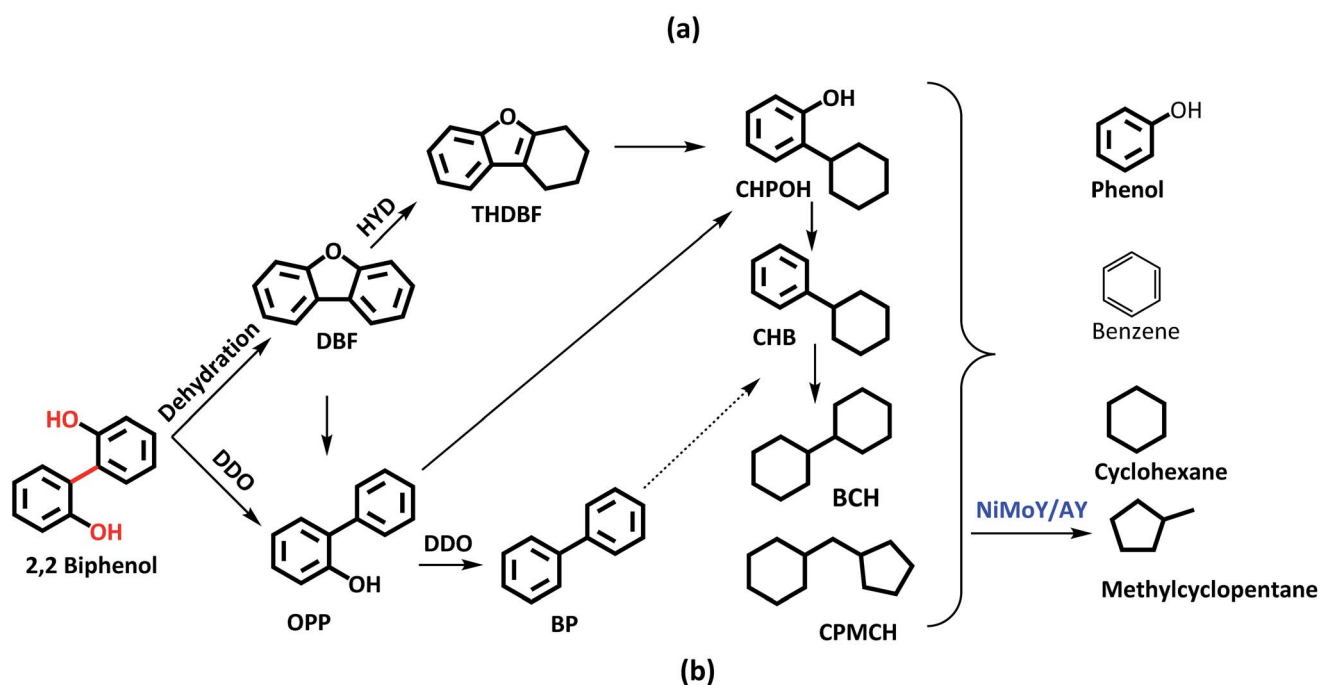


Fig. 4 (a) Product selectivity's during HDO of 2,2'-biphenol over NiMoA, NiMoAY and NiMoY and (b) proposed reaction scheme during HDO of 2,2'-biphenol.

Table 4 ICP data-metal contents on synthesized and spent catalysts

Catalyst	As-synthesized				After the BPE test		After the PPE test		After the 5-5' test	
	Mo (wt%)	Ni (wt%)	Si/Al	Ni/(Ni + Mo)	Si/Al	Ni/(Ni + Mo)	Si/Al	Ni/(Ni + Mo)	Si/Al	Ni/(Ni + Mo)
Y	—	—	15.0 ^a	—	—	—	—	—	—	—
NiMoA	13.3	4.6	—	0.26	—	0.28	—	0.26	—	0.24
NiMoAY	12.3	4.4	0.6	0.27	0.71	0.27	0.65	0.27	0.62	0.26
NiMoY	13.2	4.8	16.5	0.27	13.5	0.27	13.3	0.28	16.4	0.28

^a Zeolyst international.



Table 6 N₂ physisorption data for fresh and spent catalysts^a

Catalyst	As synthesized			After the BPE test			After the PPE test			After the 5-5' test		
	S _a	V _p	d _p	S _a	V _p	d _p	S _a	V _p	d _p	S _a	V _p	d _p
γ-Al ₂ O ₃	199	0.48	97.6									
USY	763	0.25	63.3									
NiMoA	139	0.31	87.6	111	0.18	84.9	119	0.20	79.1	128	0.26	78
NiMoAY	270	0.26	71.9	163	0.18	43.8	148	0.19	51.8	175	0.23	51.9
NiMoY	412	0.20	53.1	291	0.20	27.6	246	0.20	31.9	—	—	—

^a S_a = BET surface area (m² g⁻¹), V_p = pore volume (cm³ g⁻¹), and d_p = average pore size for mesopores (Å).

Table 7 Elemental contents of carbon, hydrogen and sulfur on the freshly sulfided and spent catalysts^a

Catalyst	Freshly sulfided			After the BPE test			After the PPE test			After the 5-5' test		
	C	H	S	C*	H	S	C*	H	S	C*	H	S
NiMoA	0.4	1.3	8.8	0.98	0.8	7.7	2.1	0.7	8.2	2.7	0.5	8.3
NiMoAY	—	—	8.3	2.1	1.5	6.2	4.0	0.6	7.8	3.7	0.4	7.0
NiMoY	1.0	0.9	9.8	6.5	1.6	7.1	7.9	0.5	8.9	6.7	0.5	7.0

^a C values for catalysts after reaction tests are in (g carbon)/(g catalyst)/(mol of feed converted to deoxygenated products). All other values are in wt% including C in the sulfide catalyst.

related to the higher diffusion resistance of the larger PPE compound in the zeolite structure compared to the other model compounds. Differences in the H content between the fresh and spent catalysts are negligible, whereas there is only a minor decrease in the S content of the spent catalysts.

Raman spectra of the synthesized catalysts are presented in Fig. 7. The main peak for all prepared catalysts appeared at around 953 cm⁻¹. This corresponds to the symmetric stretching vibration of Mo=O in octahedrally coordinated Mo oxide species which are considered to interact weakly with the support.⁷² Such weak interaction enables the formation of highly reducible species and should enhance the activity of the catalyst. Despite a slight shift of the main peak for NiMoAY, all catalysts have similar metal-support interaction. However, peak shoulders observed at different points indicate the presence of bulk MoO₃ phases (995 cm⁻¹), less active or inactive tetrahedrally coordinated Mo oxide species (900 cm⁻¹) and the Mo–O–Mo vibration of orthorhombic MoO₃, inferring the presence of polymerized Mo oxides (825 cm⁻¹). The absence of the bulk MoO₃ peak shoulder at around 995 cm⁻¹ for the more acidic supported catalysts (NiMoAY and NiMoY) implies that they contain more easily reducible Mo oxide species.

XPS analysis of the sulfided NiMoA and NiMoY is shown in Fig. 8. Evaluation of the Ni 2p and Mo 3d core level spectra infers how the support acidity influences the sulfidation of Mo and Ni. Mo 3d spectral fitting values are: Mo⁴⁺ (MoS₂) 228.7 ± 0.1 eV for Mo 3d_{5/2} and 231.9 ± 0.1 eV for Mo 3d_{3/2}; Mo⁵⁺ (MoO₃) 232.2 ± 0.1 eV for Mo 3d_{5/2} and 235.4 ± 0.1 eV for Mo 3d_{3/2}. Ni 2p spectral fitting and deconvolution show the presence of NiS_x, NiMoS and Ni²⁺ species at 852.8 ± 0.1, 854.3 ± 0.1 and 856 ± 0.2 eV binding energies respectively. Mo sulfidation was calculated

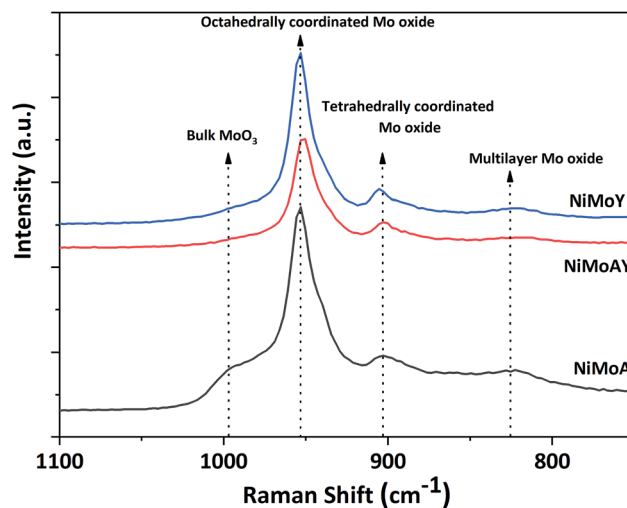


Fig. 7 Raman spectra of the synthesized catalyst.

as the contribution of Mo⁴⁺ relative to the total amount of Mo species in the Mo 3d core level spectra (excluding S 2s contribution) and Ni sulfidation as the contribution from NiS_x and NiMoS relative to the total amount of NiS_x, NiMoS and Ni²⁺. The results in Table 8 show that with the Y support, the contribution of the NiMoS phase is slightly higher than for NiMoA. This indicates that more Ni atoms are embedded into the MoS₂ slabs to form the active NiMoS phase⁷³ to a slightly better extent with the Y supported catalyst.

Overall sulfidation seems quite similar for both catalysts, and thus independent of the nature of the support. However, the degree of sulfidation may be underestimated from these results since there is a risk for some superfluous oxidation while transferring samples to the XPS chamber.

The morphologies of the metal sulfides are crucial in determining their activity and selectivity under the reaction conditions. The HRTEM images of the sulfided NiMoA and NiMoY shown in Fig. 9 revealed the dispersion of the active NiMoS phase. The average values of the slab length, number of stacks/slabs and fraction of edge Mo atoms were calculated based on 300 individual MoS₂ crystals for each sample. As seen from Table 8, a shorter slab length and higher stacking degree with the Y zeolite increase the dispersion (*f*_{Mo}) of the active phases compared to NiMoA. This means that more edge and corner sites of Mo atoms shall be accessible for the case with NiMoY.





Fig. 8 Core level XPS spectra of Ni 2p and Mo 3d for NiMoA and NiMoY.

Catalytic properties related to the activity

The characterization of the catalysts *via* TEM, Raman and XPS revealed that NiMo on Y has more active Mo species than NiMoA, due mainly to less bulk MoO₃ leading to a comparable degree of sulfidation and an improved dispersion of the active phase. Also, ethylamine-TPD showed a higher concentration of Brønsted acidity on the Y supported catalysts. This provided an enhanced hydrogenolysis of the ether linkage of BPE over NiMoY. However, for PPE the rate of hydrogenolysis is lower for the pure Y supported catalyst. Indeed, for both BPE and PPE, hydrogenolysis is faster on the mixed-support catalyst (NiMoAY) with moderate Brønsted acidity as shown in Fig. 2(a) and 3(a). However, for both cases transalkylation, recombination and acid catalyzed condensation of intermediates were significant leading to the formation of stable aliphatic C-linked phenolic/deoxygenated dimers (Fig. 2(c) and 3(c)). An acid catalyzed intramolecular dehydration reaction was also dominant for 2,2'-biphenol HDO. The combination and proximity of Mo dispersion and Brønsted acidity on NiMoY seem able to effectively cleave the intermediate C–C dimers (both deoxygenated and phenolic). Enhanced hydrocracking for BPE derived intermediates (*e.g.* DPM, BB, benzyl phenols *etc.*) to monophenols (cresols) and BTX thus leads to fewer residual dimers. PPE

derived intermediates also undergo such cracking to ethyl phenols. For 2,2'-biphenol almost no intermediate C–C dimers remained. It is also evident that methyl cyclopentane is a dominant product in the case of NiMoY for all three reactants which indicates the higher isomerization activity of this catalyst. However, the activity tests revealed that the deoxygenation/hydrogenation activity for NiMoY was lower compared to that of NiMoA/NiMoAY. This has led to different products consisting of a mixture of deoxygenated products and cycloalkanes over NiMoA while more aromatics over NiMoY for BPE, PPE and 2,2'-biphenol. The possible reasons for these differences proposed in the literature based on studies of hydroprocessing with sulfided metals on Y zeolite include: (1) stronger adsorption of oxygenates and phenolics on the zeolite surface creating a surface pool of these species, (2) inaccessibility of acidic sites in smaller micropores, (3) the longer diffusion distance between the metallic and acidic sites, *i.e.* poorer proximity of the active sites especially for the micropores of the zeolite, and (4) different morphologies of metal sulfides inside the zeolite micropores.^{74,75}

Previous studies from our group showed that the average particle size of NiMo on alumina, AY and Y-zeolite was in the range of 180–310 Å, which is much larger than that of the zeolite

Table 8 XPS and TEM characterization of the metal sulfides

Catalyst	Mo sulfidation (%)		Ni sulfidation (%)			Slab length (nm)	Stacking	f_{Mo}
	Mo ⁴⁺		NiS _x	NiMoS	Ni ²⁺			
NiMoA	84		16	54	30	4.7	3.8	0.22
NiMoY	82		8	61	31	4.1	4.2	0.27





Fig. 9 Characteristic HRTEM images of NiMoA and NiMoY: insets show the differences in slab distribution.

supercage of 12 Å.⁵⁵ This implies that a portion of particles will remain at the grain boundaries on the external surfaces of the micropore, but parts could be inside the grain and may even not be sulfided.⁷⁶ The fraction inside grains will be less accessible to the reactants/intermediates. Fig. 10(a) shows the yield of the intermediate phenolic dimers formed during HDO of BPE and PPE over NiMoA and NiMoY. These phenolic dimers are formed from transalkylation and recombination reactions as discussed above. First it can be noted that for the PPE feed the yields of phenolic dimers (2-phenylethylphenols) are higher for NiMoY during the entire reaction period (Fig. 10(a)), whereas for BPE the phenolic dimers (benzyl phenols) are only initially higher for NiMoY. This is likely due to the greater acidity of NiMoY catalyzing transalkylation and dehydration/condensation

reactions to form more dimers. For BPE, the intermediate benzyl phenol dimers reached a lower peak yield indicating that they could be converted more rapidly as they should be more accessible to the zeolite micropores than PPE dimers to be cracked to form smaller molecules. For PPE, the formation of 2-phenylethylphenol dimers showed a peak of higher maximum yield after around 3 h, which corresponds to when all the PPE has converted (see Fig. 3(a)), followed by a steep decrease. This indicates that the diffusion limitations play a role for both BPE and PPE; however they are more prominent for PPE and its dimers due to their larger molecular size. The diffusion limitations and pore mouth blockage create a larger surface phenolics pool. As noticed, the degree of hydrocracking/deoxygenation increases over NiMoY once the BPE/PPE are converted.



Fig. 10 (a) Yield of the intermediate phenolic dimers and benzyl phenols from BPE and 2-phenylethylphenols from PPE; (b) deoxygenated dimers from BPE and PPE.



However, the greater surface coverage by recombined dimers and phenolics on NiMoY delays the monophenol deoxygenation on metallic or acid sites due to competitive adsorption in the presence of hydrogen, *i.e.* via hydrogen transfer reaction.⁷⁷ The reactive phenolics on the NiMoY surface thus may have longer residence times that favor undesirable reactions that can deactivate the catalyst with carbonaceous products. Both BPE and PPE treated NiMoY spent catalyst samples contain around 14 wt% C, most probably due to strongly adsorbed phenolics and other carbonaceous deposits.

The phenolic dimer compounds can undergo C–C cleavage reactions to yield monophenols and aromatics or they may undergo HDO to yield deoxygenated dimers. Fig. 10(b) compares the yields of the deoxygenated dimers with NiMoY and NiMoA catalysts for both BPE and PPE. For BPE, there is a remarkable difference where the yield of deoxygenated dimers steadily increases for NiMoA, whereas it rapidly decreases after about 60 min for NiMoY. For PPE, the yield of deoxygenated dimers steadily increases for both catalysts, but at a lower rate for NiMoY. The comparison of the yields of phenolic dimers in Fig. 10(a) and deoxygenated dimers in Fig. 10(b) indicates that for NiMoA, the phenolic dimers mainly undergo HDO, whereas for the NiMoY catalyst C–C bond cleavage reactions are more favored. It is therefore evident from the HDO of BPE and PPE that the NiMoY catalyst can efficiently cleave both etheric and recombined C–C linkages while for the NiMoA C–C dimer yields only increase with time (Fig. 10). Also, the recalcitrant 5,5' linkages can be partially cleaved with NiMoY. This shows the potential of this catalyst (NiMoY) for upgrading technical lignin in future biorefineries. However, a suitable balance between the Brønsted acid sites (BASs), deoxygenation sites and pore accessibility is the key parameter essential to optimize the performance of NiMoY.

Conclusions

The support acidity of NiMo based catalysts is an effective tool to control product selectivity during the conversion of lignin feedstocks containing α -O-4, β -O-4 and C–C linkages into high value fuel additives and chemicals. NiMo on a modified support (AY) shows enhanced hydrogenolysis of etheric bonds for both BPE and PPE. With BPE, containing an α -O-4 linkage, NiMoY selectively yields more deoxygenated aromatics with fewer residual C–C dimers. For example, NiMoY produced less than 1% cyclohexane and instead formed 35% benzene, while NiMoA produced 38% cyclohexane. With PPE, containing β -O-4 linkages, NiMoA yields more ethylbenzene and cyclohexane while NiMoY favors deoxygenated aromatics including benzene, toluene, and ethylbenzene, but also produces more residual phenolics. Also, the Y-zeolite based sulfided NiMo catalyst can break the C–C linkage in 2,2'-biphenol without the formation of residual C–C dimers which were observed with NiMoA. Increased isomerization and hydrocracking activity of NiMoY can be attributed to better dispersion of the active metal sulfide phases and the presence of more and stronger Brønsted acidic sites. However, the Y-based catalyst suffered from lower phenolic deoxygenation activity that appeared to be related to

its higher initial activity for the formation of phenolic dimers and diffusion limitations. Also, a higher rate of coke formation was observed for the Y-based catalyst which may lead to faster catalyst deactivation. Hence, the proximity of the deoxygenation and acidic sites and their accessibility to the reactant/intermediates likely plays a key role for the product selectivity during HDO on NiMo based catalysts on Y-zeolites.

Conflicts of interest

There are no conflicts to declare.

Acknowledgements

This work is performed at the Competence Centre for Catalysis (KCK) and division of chemical reaction engineering at the Chalmers University of Technology. We would like to acknowledge the Swedish Energy Agency (contract: 2016-08330) for the financial aid. We would also like to acknowledge Stefan Gustafsson for his help with the TEM analysis.

Notes and references

- H. Wang, H. Ruan, M. Feng, Y. Qin, H. Job, L. Luo, C. Wang, M. H. Engelhard, E. Kuhn, X. Chen, M. P. Tucker and B. Yang, *ChemSusChem*, 2017, **10**, 1846–1856.
- J. Zakzeski, P. C. A. Bruijninx, A. L. Jongerius and B. M. Weckhuysen, *Chem. Rev.*, 2010, **110**, 3552–3599.
- S. Guadix-Montero and M. Sankar, *Top. Catal.*, 2018, **61**, 183–198.
- A. V. Bridgwater, *Biomass Bioenergy*, 2012, **38**, 68–94.
- E. L. a. B. Delmon, *Ind. Eng. Chem. Res.*, 1993, **32**, 2516–2524.
- C. Zhao, J. He, A. A. Lemonidou, X. Li and J. A. Lercher, *J. Catal.*, 2011, **280**, 8–16.
- B. Yoosuk, D. Tumnantong and P. Prasassarakich, *Chem. Eng. Sci.*, 2012, **79**, 1–7.
- S. Echeandia, B. Pawelec, V. L. Barrio, P. L. Arias, J. F. Cambra, C. V. Loricera and J. L. G. Fierro, *Fuel*, 2014, **117**, 1061–1073.
- H. Shafaghat, P. S. Rezaei and W. M. Ashri Wan Daud, *RSC Adv.*, 2015, **5**, 103999–104042.
- C. Newman, X. Zhou, B. Goundie, I. T. Ghampson, R. A. Pollock, Z. Ross, M. C. Wheeler, R. W. Meulenberg, R. N. Austin and B. G. Frederick, *Appl. Catal., A*, 2014, **477**, 64–74.
- S. Boullousa-Eiras, R. Lødeng, H. Bergem, M. Stöcker, L. Hannevold and E. A. Blekkan, *Catal. Today*, 2014, **223**, 44–53.
- L. T. Funkenbusch, M. E. Mullins, M. A. Salam, D. Creaser and L. Olsson, *Fuel*, 2019, **243**, 441–448.
- X. Zhu, L. L. Lobban, R. G. Mallinson and D. E. Resasco, *J. Catal.*, 2011, **281**, 21–29.
- Q. Tan, G. Wang, A. Long, A. Dinse, C. Buda, J. Shabaker and D. E. Resasco, *J. Catal.*, 2017, **347**, 102–115.
- I. T. Ghampson, G. Pecchi, J. L. G. Fierro, A. Videla and N. Escalona, *Appl. Catal., B*, 2017, **208**, 60–74.



- 16 D. Shi, L. Arroyo-Ramírez and J. M. Vohs, *J. Catal.*, 2016, **340**, 219–226.
- 17 V. N. Bui, D. Laurenti, P. Afanasiev and C. Geantet, *Appl. Catal., B*, 2011, **101**, 239–245.
- 18 I. D. Mora, E. Méndez, L. J. Duarte and S. A. Giraldo, *Appl. Catal., A*, 2014, **474**, 59–68.
- 19 I. D. Mora-Vergara, L. Hernández Moscoso, E. M. Gaigneaux, S. A. Giraldo and V. G. Baldovino-Medrano, *Catal. Today*, 2018, **302**, 125–135.
- 20 Z. He, M. Hu and X. Wang, *Catal. Today*, 2018, **302**, 136–145.
- 21 Z. Luo, Z. Zheng, Y. Wang, G. Sun, H. Jiang and C. Zhao, *Green Chem.*, 2016, **18**, 5845–5858.
- 22 X. Zhang, T. Wang, L. Ma, Q. Zhang, Y. Yu and Q. Liu, *Catal. Commun.*, 2013, **33**, 15–19.
- 23 E. Laurent and B. Delmon, *Appl. Catal., A*, 1994, **109**, 97–115.
- 24 X. Lan, E. J. M. Hensen and T. Weber, *Appl. Catal., A*, 2018, **550**, 57–66.
- 25 H. Y. Zhao, D. Li, P. Bui and S. T. Oyama, *Appl. Catal., A*, 2011, **391**, 305–310.
- 26 T. R. H. Douglas and C. Elliott, *Energy Fuels*, 2009, **23**, 631–637.
- 27 M. Alda-Onggar, P. Maki-Arvela, K. Eranen, A. Aho, J. Hemming, P. Paturi, M. Peurla, M. Lindblad, I. L. Simakova and D. Y. Murzin, *ACS Sustainable Chem. Eng.*, 2018, **6**, 16205–16218.
- 28 X. Liu, W. Jia, G. Xu, Y. Zhang and Y. Fu, *ACS Sustainable Chem. Eng.*, 2017, **5**, 8594–8601.
- 29 P. E. Ruiz, B. G. Frederick, W. J. De Sisto, R. N. Austin, L. R. Radovic, K. Leiva, R. García, N. Escalona and M. C. Wheeler, *Catal. Commun.*, 2012, **27**, 44–48.
- 30 X. Li, G. Chen, C. Liu, W. Ma, B. Yan and J. Zhang, *Renewable Sustainable Energy Rev.*, 2017, **71**, 296–308.
- 31 M. Saidi, F. Samimi, D. Karimipourfard, T. Nimmanwudipong, B. C. Gates and M. R. Rahimpour, *Energy Environ. Sci.*, 2014, **7**, 103–129.
- 32 M. Koyama, *Bioresour. Technol.*, 1993, **44**, 209–215.
- 33 A. L. Jongorius, R. Jastrzebski, P. C. A. Bruijninx and B. M. Weckhuysen, *J. Catal.*, 2012, **285**, 315–323.
- 34 B. Güvenatam, O. Kurşun, E. H. J. Heeres, E. A. Pidko and E. J. M. Hensen, *Catal. Today*, 2014, **233**, 83–91.
- 35 C. Zhao and J. A. Lercher, *Angew. Chem., Int. Ed.*, 2012, **51**, 5935–5940.
- 36 W. Zhang, J. Chen, R. Liu, S. Wang, L. Chen and K. Li, *ACS Sustainable Chem. Eng.*, 2014, **2**, 683–691.
- 37 Y.-K. Hong, D.-W. Lee, H.-J. Eom and K.-Y. Lee, *Appl. Catal., B*, 2014, **150–151**, 438–445.
- 38 W. Schutyser, T. Renders, S. Van den Bosch, S. F. Koelewijn, G. T. Beckham and B. F. Sels, *Chem. Soc. Rev.*, 2018, **47**, 852–908.
- 39 W. Song, S. Zhou, S. Hu, W. Lai, Y. Lian, J. Wang, W. Yang, M. Wang, P. Wang and X. Jiang, *ACS Catal.*, 2018, **9**, 259–268.
- 40 L. Shuai, J. Sitison, S. Sadula, J. Ding, M. C. Thies and B. Saha, *ACS Catal.*, 2018, **8**, 6507–6512.
- 41 S. Mukundan, L. Atanda and J. Beltramini, *Sustainable Energy Fuels*, 2019, **3**, 1317–1328.
- 42 M. Williams, B. Fonfe, C. Sievers, A. Abraham, J. Vanbokhoven, A. Jentys, J. Vanveen and J. Lercher, *J. Catal.*, 2007, **251**, 485–496.
- 43 J. García-Martínez, M. Johnson, J. Valla, K. Li and J. Y. Ying, *Catal. Sci. Technol.*, 2012, **2**, 987–994.
- 44 Z. Ma, E. Troussard and J. A. van Bokhoven, *Appl. Catal., A*, 2012, **423–424**, 130–136.
- 45 J. Garcia-Martinez, K. Li and G. Krishnaiah, *Chem. Commun.*, 2012, **48**, 11841–11843.
- 46 S. G. A. Ferraz, B. M. Santos, F. M. Z. Zotin, L. R. R. Araujo and J. L. Zotin, *Ind. Eng. Chem. Res.*, 2015, **54**, 2646–2656.
- 47 S. G. A. Ferraz, F. M. Z. Zotin, L. R. R. Araujo and J. L. Zotin, *Appl. Catal., A*, 2010, **384**, 51–57.
- 48 J.-I. Park, J.-K. Lee, J. Miyawaki, Y.-K. Kim, S.-H. Yoon and I. Mochida, *Fuel*, 2011, **90**, 182–189.
- 49 M. O. Kazakov, K. A. Nadeina, I. G. Danilova, P. P. Dik, O. V. Klimov, V. Y. Pereyema, E. A. Paukshtis, I. S. Golubev, I. P. Prosvirin, E. Y. Gerasimov, I. V. Dobryakova, E. E. Knyazeva, I. I. Ivanova and A. S. Noskov, *Catal. Today*, 2019, **329**, 108–115.
- 50 D. Y. Hong, S. J. Miller, P. K. Agrawal and C. W. Jones, *Chem. Commun.*, 2010, **46**, 1038–1040.
- 51 H. Lee, H. Kim, M. J. Yu, C. H. Ko, J. K. Jeon, J. Jae, S. H. Park, S. C. Jung and Y. K. Park, *Sci. Rep.*, 2016, **6**, 28765.
- 52 A. K. Deepa and P. L. Dhepe, *RSC Adv.*, 2014, **4**, 12625–12629.
- 53 M. Abdus Salam, D. Creaser, P. Arora, S. Tamm, E. Lind Grennfelt and L. Olsson, *Catalysts*, 2018, **8**, 418.
- 54 P. Arora, H. Ojagh, J. Woo, E. Lind Grennfelt, L. Olsson and D. Creaser, *Appl. Catal., B*, 2018, **227**, 240–251.
- 55 H. Ojagh, D. Creaser, M. A. Salam, E. L. Grennfelt and L. Olsson, *Fuel Process. Technol.*, 2019, **190**, 55–66.
- 56 W. Zhou, Y. Zhou, Q. Wei, L. Du, S. Ding, S. Jiang, Y. Zhang and Q. Zhang, *Chemistry*, 2017, **23**, 9369–9382.
- 57 J. He, L. Lu, C. Zhao, D. Mei and J. A. Lercher, *J. Catal.*, 2014, **311**, 41–51.
- 58 X.-Y. Wei, E. Ogata, Z.-M. Zong and E. Niki, *Energy Fuels*, 1992, **6**, 868–869.
- 59 W.-C. Cheng and K. Rajagopalan, *J. Catal.*, 1989, **119**, 354–358.
- 60 S. Krishnamurthy, S. Panvelker and Y. T. Shah, *AIChE J.*, 1989, **27**, 994–1001.
- 61 J. Zhang, C. Li, X. Chen, W. Guan and C. Liang, *Catal. Today*, 2019, **319**, 155–163.
- 62 J. Zhang, C. Li, X. Chen, Y. Chen, L. Zhang, B. Zhang and C. Liang, *J. Catal.*, 2019, **371**, 346–356.
- 63 J. Zhang, L. Wang, C. Li, S. Jin and C. Liang, *Org. Process Res. Dev.*, 2018, **22**, 67–76.
- 64 L. Wang, H. Wan, S. Jin, X. Chen, C. Li and C. Liang, *Catal. Sci. Technol.*, 2015, **5**, 465–474.
- 65 O. A. Abdelrahman, K. P. Vinter, L. Ren, D. Xu, R. J. Gorte, M. Tsapatsis and P. J. Dauenhauer, *Catal. Sci. Technol.*, 2017, **7**, 3831–3841.
- 66 O. Kresnawahjuesa, R. J. Gorte, D. d. Oliveira and L. Y. Lau, *Catal. Lett.*, 2002, **82**, 155–160.
- 67 R. J. Gorte, *Catal. Lett.*, 1999, **62**, 1–13.
- 68 H. H. Ingelsten, M. Skoglundh and E. Fridell, *Appl. Catal., B*, 2003, **41**, 287–300.



- 69 A. Wang, B. Lin, H. Zhang, M. H. Engelhard, Y. Guo, G. Lu, C. H. F. Peden and F. Gao, *Catal. Sci. Technol.*, 2017, 7, 2362–2370.
- 70 K. Sato, Y. Nishimura and H. Shimada, *Catal. Lett.*, 1999, 60, 83–87.
- 71 O. İ. Şenol, T. R. Viljava and A. O. I. Krause, *Appl. Catal., A*, 2007, 326, 236–244.
- 72 N. Kunisada, K.-H. Choi, Y. Korai, I. Mochida and K. Nakano, *Appl. Catal., A*, 2004, 269, 43–51.
- 73 W. Zhou, M. Liu, Q. Zhang, Q. Wei, S. Ding and Y. Zhou, *ACS Catal.*, 2017, 7, 7665–7679.
- 74 E. J. M. Hensen and J. A. R. van Veen, *Catal. Today*, 2003, 86, 87–109.
- 75 K. Sato, Y. Nishimura, K. Honna, N. Matsubayashi and H. Shimada, *J. Catal.*, 2001, 200, 288–297.
- 76 M. J. M. Leglise, C. Potvin, G. Djega-Mariadassou and D. Cornet, *J. Catal.*, 1995, 152, 275–290.
- 77 M. Heuchel, C. Dörr, R. Boldushevskii, S. Lang, E. Klemm and Y. Traa, *Appl. Catal., A*, 2018, 553, 91–106.

